Chemical Engineering Journal 370 (2019) 444–454

Contents lists available at ScienceDirect

Chemical Engineering Journal

journal homepage: www.elsevier.com/locate/cej

Internal flow patterns of a droplet pinned to the hydrophobic surfaces of a confined microchannel using micro-PIV and VOF simulations

Guang Yang[a,b,*], Alexandros Terzis[b,*], Ioannis Zarikos[c], S. Majid Hassanizadeh[c], Bernhard Weigand[b], Rainer Helmig[d]

[a] Institute of Refrigeration and Cryogenics, School of Mechanical Engineering, Shanghai Jiao Tong University, 200240 Shanghai, China
[b] Institute of Aerospace Thermodynamics, University of Stuttgart, 70569 Stuttgart, Germany
[c] Environmental Hydrogeology Group, Department of Earth Sciences, Utrecht University, 3584 CD Utrecht, The Netherlands
[d] Department of Hydromechanics and Modelling of Hydrosystems, University of Stuttgart, 70569 Stuttgart, Germany

HIGHLIGHTS

- Droplets can be pinned to solid surfaces at low Ca due to contact angle hysteresis.
- The internal circulation of the droplet is observed and quantified by micro-PIV.
- The internal flow patterns are simulated successfully with modified VOF method.
- The force model for the pinned droplet in the microchannel is built and improved.
- The internal circulation intensity of the droplet is found to vary linearly with Ca.

ARTICLE INFO

Keywords:
Contact angle hysteresis
Contact line dynamics
Droplet
Microfluidics
Micro-PIV
Volume of fluid

ABSTRACT

We present both experimental results and numerical simulations of the fluid dynamics of a droplet pinned to the hydrophobic surfaces of a confined microfluidic channel, as a result of contact angle hysteresis. Internal circulations in the droplet are observed and quantified using micro-particle image velocimetry (μPIV). As the channel inlet velocity increases, the difference between the contact angles at the front and the rear part of the contact line is also increased, while the equilibrium Young's contact angle remains essentially constant. Numerical simulations based on a Volume-Of-Fluid (VOF) method combined with a Laplacian filter for the phase function are also performed to consider contact angle hysteresis effects. Major quantities from the simulations, including the velocity distribution inside the droplet, the contact angles, and the vortex structures, show good agreement with experimental results. In addition, force balance models of the pinned droplet have been built for various inlet conditions, indicating that the adhesion force at the side walls and the blockage of the droplet have significant effects on the liquid motion within the droplet. The recirculation flow rate inside the droplet is found to vary linearly with the Capillary number.

1. Introduction

Droplet dynamics during viscous flow of an immiscible fluid is a characteristic feature of numerous applications including self-cleaning surfaces [1], cell movement in blood flow [2], membrane emulsification [3], water removal in fuel cells [4], spray coating [5], and petroleum engineering [6]. In addition, scientific interest in droplet-based microfluidics has been rapidly growing over the past few decades because droplet motion on solid surfaces is widely controlled for applications that involve droplet generation, mixing, and manipulation [7,8].

A liquid droplet attached to the solid surface within an immiscible channel flow exhibits various dynamic behaviours because its static contact angle is subject to a hysteresis effect. The latter is characterized by a spectrum of contact angles ranging from the advancing contact angle (θ_A) to the receding one (θ_R), while the difference between the two ($\theta_A - \theta_R$) is a measure of the contact angle hysteresis [9]. Because the droplet is exposed to a channel flow, the external drag force acting

* Corresponding authors at: Institute of Refrigeration and Cryogenics, School of Mechanical Engineering, Shanghai Jiao Tong University, 200240 Shanghai, China (G. Yang).
E-mail addresses: y_g@sjtu.edu.cn (G. Yang), alexandros.terzis@me.com (A. Terzis).

https://doi.org/10.1016/j.cej.2019.03.191
Received 19 November 2018; Received in revised form 22 February 2019; Accepted 20 March 2019
Available online 22 March 2019
1385-8947/

Nomenclature

Nomenclature

$\hat{\mathbf{e}}$	direction vector
$\hat{\mathbf{n}}$	normal vector
A	area, m^2
Bn	Bond number
C_D	drag coefficient
Ca	Capillary number
Co	Courant number
E_d	projection area, m^2
F	force, N
g	gravity acceleration, m/s^2
H	channel height, m
h	droplet height, m
P	pressure, Pa
Q	volume flow rate, m^3/s
r	radius of droplet, m
Re	Reynolds number
S	contact line, m
t	time, s
U	velocity, m/s
We	Weber number
x, y, z	Cartesian coordinate system, m

Greek Symbols

α	phase fraction
Δ	grid size, m
γ	surface/interface tension, N/m
κ	curvature
μ	viscosity, kg/(m s)
ρ	density, kg/m^3
θ	contact angle, deg

Superscript

i	quasi-state

Subscript

A	advancing
E	equilibrium
in	inlet condition
l	liquid
m	mass center of the droplet
w	wetting phase
R	receding
r	reversed flow
s	solid
nw	non-wetting phase

on its surface modifies the adhesion force on the contact line, whose effect is compensated by the contact angle hysteresis and the surface tension of the droplet fluid. Therefore, the droplet may deform by altering the contact angles at the contact lines. If the velocity of the channel flow is small enough, so that the contact angle of the droplet lies in the range between θ_A and θ_R, the contact line will remain in a stationary condition and the droplet will be pinned to the surface. However, as the external force increases and the contact angle exceeds that range, the droplet will roll, slide, oscillate, or even break up into smaller ones [10–12].

The determination of critical conditions for different models of droplet motion on a solid surface has been widely studied in the literature. For example, the critical Capillary number for drop removal has been experimentally found to be a function of the contact angle hysteresis, the channel dimensions, the surface tension force, the viscosity ratio, the initial shape of the droplet, and other factors [13–19]. Thampi et al. [20] investigated the motion of a two-dimensional (2D) droplet on an inclined surface. Under gravity conditions, the authors characterized the sliding versus the rolling motion of the droplet by decomposing the velocity gradient inside the droplet into a shear flow and a residual flow. Cho et al. [21] analyzed, both numerically and theoretically, water droplet dynamics in a gas flow channel, and an expression relating the Weber number ($We = \rho U^2 r/\gamma$) to the Reynolds number was developed by comparing the wall adhesion and drag forces. Xie et al. [22] theoretically established two criteria to determine the onset of drop sliding and rolling, including dimensionless numbers such as the Bond number ($Bn = (\rho_1 - \rho_2)gr^2/\gamma$), the Ohnesorge number ($Oh = \mu_1/(\sqrt{\rho\sigma r})$), and the Weber number, as well as the inclination angle. The motion mode was found to depend only on the equilibrium contact angle (θ_E), where droplet rolling occurred at $\theta_E > 147°$.

Apparently, most studies available in the literature focus on the overall movement or the shape deformation of the droplet. However, the internal flow patterns of the droplet, which are of vital importance for accurate fluid handling in droplet-based microfluidic devices or relevant systems [23], have not been adequately investigated. Annapragada et al. [24] studied the rolling motion of a droplet down an inclined plane using a 2D Volume-Of-Fluid (VOF) Continuous Surface Force (CSF) model that was found to predict well the experimentally determined terminal velocity and the shape of the droplet. Although the results reported the droplet rolling phenomenon, the detailed velocity vectors inside the droplet were not obtained experimentally. The internal fluid dynamics of a water droplet on an inclined hydrophobic surface were also examined by Yilbas et al. [25,26], using particle-image-velocimetry (PIV) and high-speed imaging. The influence of droplet size and inclination angle on the droplet rotational speed were examined, providing very useful information on the droplet velocity field. However, the droplet motion regime on an inclined surface is different than that in a typical microchannel. The main difference is attributed to the driving force of the motion, which is gravity for the inclined surface and the drag force induced by the surroundings for microchannel flow. Furthermore, because of the low Eötvös number [27], the force of gravity in micro-scale applications can be neglected if the droplet diameter is on the order of a few hundred micrometers. Zarikos et al. [19] investigated experimentally the velocity distributions in trapped and mobilised non-wetting phase globules in porous media. The authors demonstrated that the interplay of capillarity and momentum transfer between the two fluid phases, is the main factor in internal recirculation of the globule that is more pronounced at fluid–fluid interfaces. Kinoshita et al. [28] measured the internal flow of a small droplet traveling through a microchannel generated from a T-junction using a confocal micro-PIV system, which indicated that the fluid inside a droplet circulates intricately. A similar test for such a physical model was performed by Liu et al. [29] for micro-droplets traveling in a microchannel, while internal recirculation patterns have been also observed in segmented multiphase flow conditions [30].

This study examines the deformation and the fluid dynamics inside a water droplet adhering to the hydrophobic solid surfaces of a confined micro-channel. A micro-PIV system is used to measure the internal fluid dynamics of a water droplet, from the pinned state to the occurrence of droplet mobilisation. The internal rotation of a droplet pinned to hydrophobic surfaces is experimentally observed and quantified. Numerical simulations are also performed using a VOF method. The accuracy of the numerical models is assessed by a comparison of key quantities with experimental results. A force analysis is performed for

the pinned droplet under various inlet conditions. The rest of this paper is organised as follows: In Section 2, the experimental method is introduced. In Section 3, the droplet motion obtained by experiments and some physical insights are described. In Section 4, the numerical approach is described, and some numerical parameters are provided. In Section 5, the numerical results are discussed and compared with the experiments. A force balance analysis is performed, and the intensity of the internal circulation of the droplet is studied in Sections 6 and 7, respectively, based on the simulation results. The paper closes with some key conclusions in Section 8.

2. Experimental method

The experiments were conducted in a T-junction micromodel made of polydimethylsiloxane (PDMS) that was fabricated based on a standard soft lithography technique [31,32]. A schematic representation of the micromodel is shown in Fig. 1(a). The height and depth of the channel are 200 and 50 μm, respectively, resulting in an aspect ratio of 4 for the channel cross-sectional area. The length of the channel from the T-junction to the drain exit tube is 20 mm. This allowed the desirable formation of a droplet, while also providing adequate length for its subsequent observation.

The channel was initially saturated with the *wetting phase* (Fluorinert FC-43, 15 mN/m, 1860 Kg/m^3, 4.7 mPa·s) and then, the *non-wetting phase* (distilled water, 72.8 mN/m, 998 Kg/m^3, 1 mPa·s), was slowly introduced through the T-junction. The droplet generation processes resulted in a flat ellipsoidally shaped droplet that was attached to the upper wall of the channel with its principal axis parallel to the channel, as shown in Fig. 1(a). This phenomenon is possible during the breakup process when the continuous phase momentum and viscosity are considerably higher than the discontinuous one [33,34]. Directly after the water droplet was pinched off, the feeding of the micromodel was briefly paused from both entries to create stagnant flow conditions, thereby generating a hydrophobic droplet inside the confined microfluidic channel. The flow rate of the wetting phase was then gradually increased until mobilisation of the water droplet occurred.

During each steady-state flow condition, the local velocity distributions inside the water droplet were obtained with a LaVision micro-PIV system equipped with a Carl Zeiss AxioObserver.Z1 microscope. The water was doped with fluorescent rhodamine 6G particles with a diameter of 0.86 µm and a density of 1.05 kg/m^3. A schematic representation of the setup is shown in Fig. 1(b). The fluorescent particles were excited at a wavelength of 542 *n*m through a Carl Zeiss HBO 100 illuminator and identified at their emitting wavelength (612 *n*m) by an IDS CMOS camera (UI-3180CP; 2592 × 2048 pixels). The velocity vectors were therefore determined from consecutive image pairs of the video sequence in MATLAB (PIVlab 1.43 [35]). The frame rate of the video was adjusted depending on the flow rate so that the maximum particle displacement in the droplet never exceeded one-quarter of the final interrogation window [36]. A double-pass algorithm was used to provide the velocity correlations. An initial window size of 128 × 128 pixels was reduced to 64 × 64 pixels and 50% window overlap. The final interrogation window size equaled about 12 × 12 µm^2, and consequently, the velocity vectors were obtained with a spatial resolution of 6 × 6 µm^2. The overall uncertainty in the determination of the velocity components was below 6%.

Because contact angle hysteresis at a solid surface could be attributed to chemical heterogeneities or roughness, an atomic force microscopy (AFM) test was also conducted to characterise the roughness effect. As shown in Fig. 2, the PDMS surface used in the experimental setup is very smooth with a root-mean-square (RMS) and R_z roughness of 1.8 *n*m and 11.5 *n*m, respectively. Consequently, the roughness has been considered to have no influence on the contact angle hysteresis [37,38].

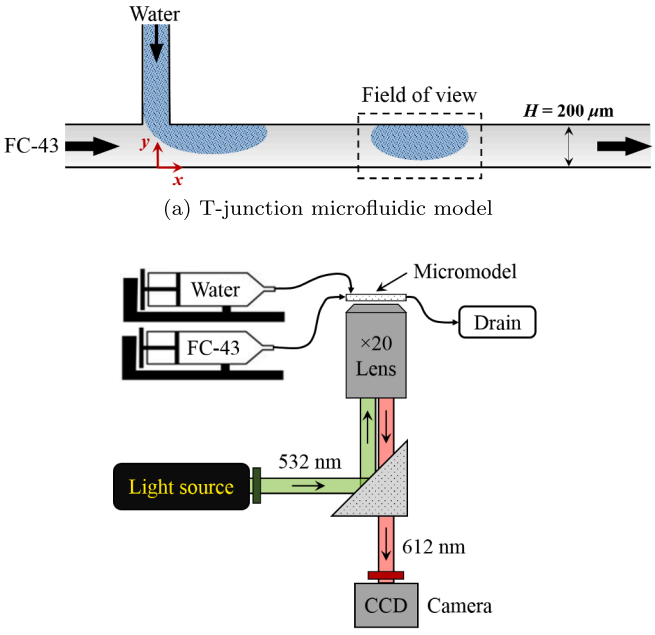

Fig. 1. Schematic representation of the experimental methodology.

3. Droplet motion

The droplet outlines for various Capillary numbers[1] are shown in Fig. 3 in the form of experimental streaklines. For all cases, a circulation of fluids is qualitatively observed inside the droplet, as specified also by the small arrows in Fig. 3 (a). As the Capillary number, *Ca*, increases, the contact line at the front part of the droplet is observed to be pinned on the surface, while the rear one moves forward (Figs. 3(b)–(g)) as pushed by the wetting-phase. Such a change in the contact line strongly differs from the case that a droplet motion is driven by gravity on an inclined plate [39], where the front contact line starts to move prior to the rear one as the external force increases. The decrease in contact area at the wall also leads to an increase in the projection area of the droplet in the channel flow direction owing to mass conservation. For a higher inlet velocity, e.g., Figs. 3(h) and (j), a critical Capillary number is reached and the droplet starts rolling away.

To quantify the droplet motion process, Fig. 4 shows the velocity vectors and distributions at the middle plane of the channel for various Capillary numbers. For all cases, the velocity vectors demonstrate a counter-clockwise rotation inside the droplet caused by the local flow pattern of the wetting phase. The maximum velocities are obtained at the throat of the liquid–liquid interface while the intensity of circulation is increased as the wetting-phase flow rate increases. In particular, for small *Ca*, e.g. Fig. 4 (a), the flow within the droplet is limited to a small region along the perimeter of the droplet. However, an increase of *Ca* leads to an inward evolution of the flow circulations. For example, Fig. 4 (d) indicates a region with a backward velocity at the non-wetting phase – solid interface. Similar results were reported by Zarikos et al. [19].

The deformation of the droplet as the wetting-phase velocity increases can be clearly observed in Fig. 5, which shows the superposition of liquid–liquid interfaces at different Capillary numbers. Interestingly,

[1] The Capillary number is defined as:

$$Ca = \mu_w \overline{U}_w / \gamma_{nw-w} \quad (1)$$

where μ_w and $\overline{U}_w$ are the dynamic viscosity and average inlet velocity of the wetting phase (FC-43), and γ_{w-nw} is the interfacial energy between wetting (*w*) and the non-wetting phases (*nw*).

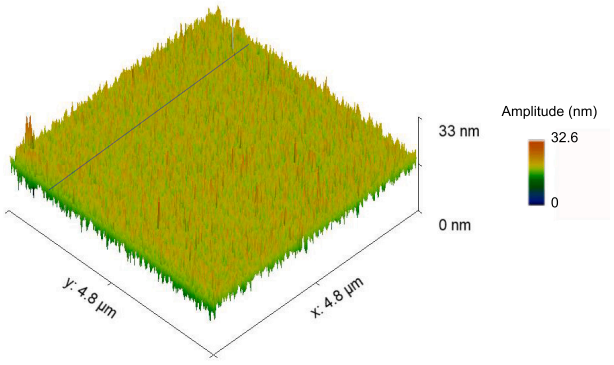

(a) Surface morphology of PDMS using Atomic Force Microscopy (AFM) for a scanned domain of $4.8 \times 4.8\ \mu m^2$

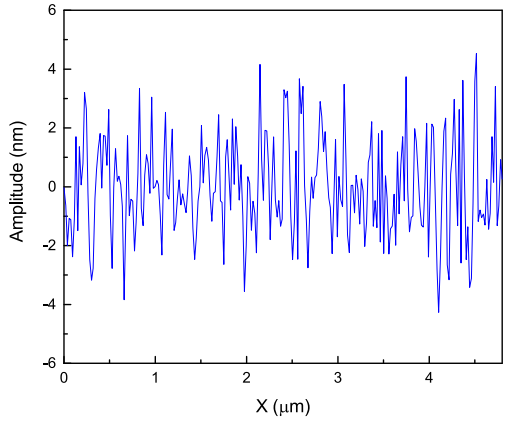

(b) Surface roughness along the marked line on the above scanned surface indicating an RMS roughness value of $1.8nm$

Fig. 2. Characterisation of PDMS surface.

the rear part of the liquid–liquid interface experiences an imbibition process while the interface at the front part of the droplet is pinned over the complete range of subcritical Capillary numbers. This forces the droplet to spread out towards the bottom of the channel with a drainage interfacial process in the region of higher velocity magnitude. These trends are in agreement with Zarikos et al. [32] who also observed a similar behaviour of the liquid-liquid interfaces during the deformation and mobilisation of trapped non-wetting phase ganglia.

To quantify the overall droplet behaviour, Fig. 6 (a) shows the variation of the various contact angles against Capillary number. Generally, as *Ca* increases, the advanced-front contact angle, θ_A^i, increases and the rear one θ_R^i decreases (*i* indicate the case where the droplet is in steady or quasi-steady state). However, the equilibrium Young's contact angle, θ_E, calculated by the model of Tadmor [9], is found to be almost a constant at about 126° for all cases, including both pinned and rolling flow situations. Note that this value is very close to the empirical equilibrium contact angle of 128.1° calculated from Young's equation ($\cos\theta_E = (\gamma_{s-w} - \gamma_{s-nw})/\gamma_{nw-w}$) combined with the following empirical model for the solid–liquid interfacial tensions [40]:

$$\gamma_{sl} = \gamma_s + \gamma_l - 2\Phi(\sqrt{\gamma_s \gamma_l}), \tag{2}$$

with Φ equal to 0.75 and 1 for the solid–water (Φ_{s-nw}) and the solid-FC-43 (Φ_{s-w}) interfaces.

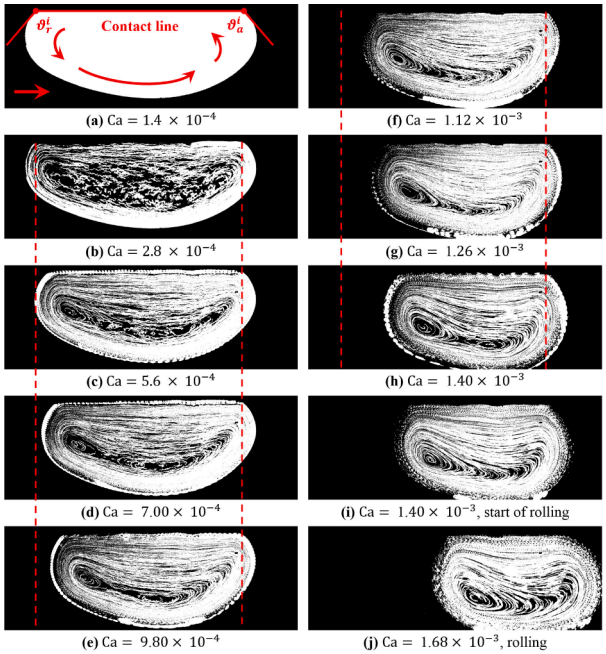

Fig. 3. Variation in droplet shape as the Capillary number is increased stepwise. (a)–(f) Fixed contact line with time; (g) and (h) moving contact line with time.

When a critical Capillary number is reached, e.g. $Ca_{cr} = 1.40 \times 10^{-3}$, the mobilisation process of the droplet takes place and the contact line starts moving with a contact line velocity. This is because the difference between θ_A^i and θ_R^i exceeds the contact angle hysteresis when $Ca > Ca_{cr}$, which breaks the force balance, as also shown in Fig. 6 (b). As *Ca* increases, $\theta_A^i - \theta_R^i$ monotonically increases to balance the drag force induced by the surrounding flow. However, the contact angles abruptly change during the motion transition from pinning to rolling. Here, it can also be found that dynamic advancing and receding contact angles and the contact angle hysteresis for the considered water-Fluorinert-PDMS interface are about 136°, 116°, and 20°, respectively.

4. Numerical methods

4.1. Governing equations and boundary conditions

All simulations were conducted based on the VOF method using the open source platform OpenFOAM (v5.0). In the VOF method, the phases were tracked with a fraction function α ($0 \leqslant \alpha \leq 1$). For a two-phase flow problem, the value of $\alpha$was 1, when a cell was filled with the disperse phase (here water); when a cell was filled with the other phase, the value of α was 0; for a fluid interface in the cell, $0 < \alpha < 1$. In this study, the two fluids were considered to be Newtonian, immiscible, incompressible, and isothermal. The surface tension force has been modelled via the CSF method by Brackbill et al. [41], the related equations can be written as follows:

$$\frac{\partial \rho}{\partial t} + \nabla \cdot \left(\rho \mathbf{U}\right) = 0, \tag{3}$$

$$\frac{\partial \rho \mathbf{U}}{\partial t} + \nabla \cdot \left(\rho \mathbf{U}\mathbf{U}\right) - \nabla \cdot \tau = -\nabla p + \gamma \kappa \nabla \alpha + \rho \mathbf{g}, \tag{4}$$

$$\frac{\partial \alpha}{\partial t} + \nabla \cdot \left(\alpha \mathbf{U}\right) + \nabla \cdot \left(\alpha\left(1 - \alpha\right)\mathbf{U}_r\right) = 0 \tag{5}$$

where γ is the surface tension coefficient (interfacial tension coefficient of water and FC-43 in this study, γ_{nw-w}) and κ is the curvature of the interface, given by

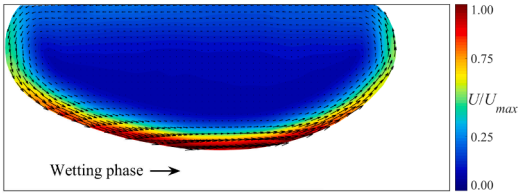

(a) $Ca = 1.40 \times 10^{-4}$

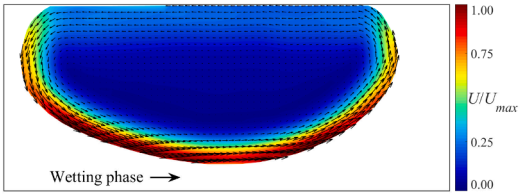

(b) $Ca = 5.60 \times 10^{-4}$

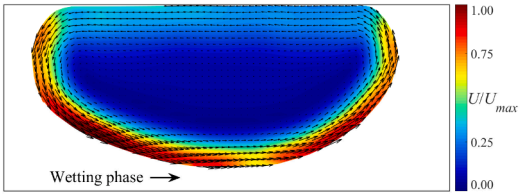

(c) $Ca = 7.00 \times 10^{-4}$

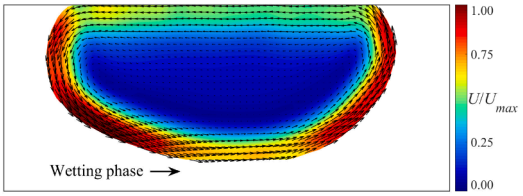

(d) $Ca = 9.8 \times 10^{-4}$

Fig. 4. Velocity distributions at the middle plane of the pinned droplets for various Capillary numbers.

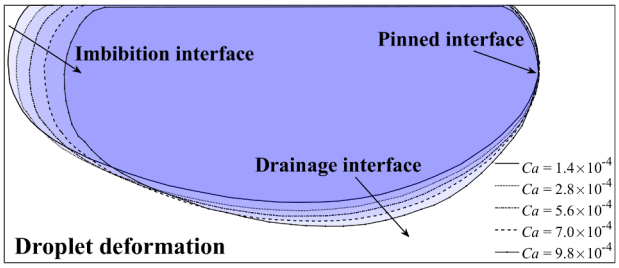

Fig. 5. Superimposed liquid–liquid interface and droplet outline deformation for different Capillary numbers.

$$\kappa = -\nabla \cdot \hat{\mathbf{n}}. \tag{6}$$

The quantity $\hat{\mathbf{n}}$ in Eq. (6) is the face-centered interface normal vector and is given by

$$\hat{\mathbf{n}} = \frac{\nabla \alpha}{|\nabla \alpha|}. \tag{7}$$

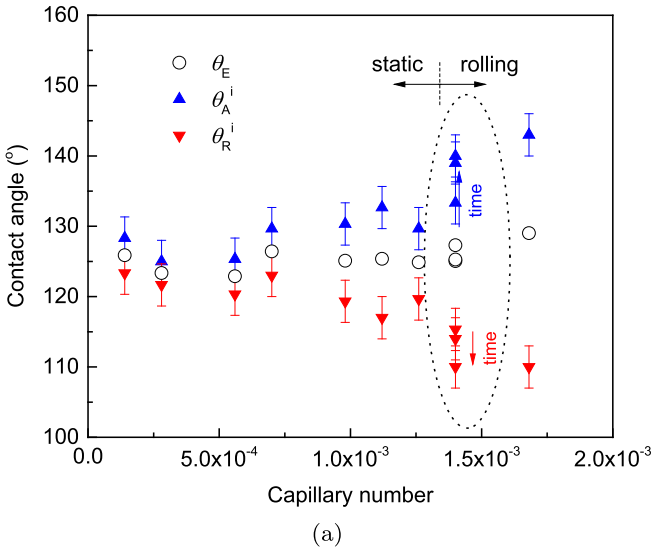

(a)

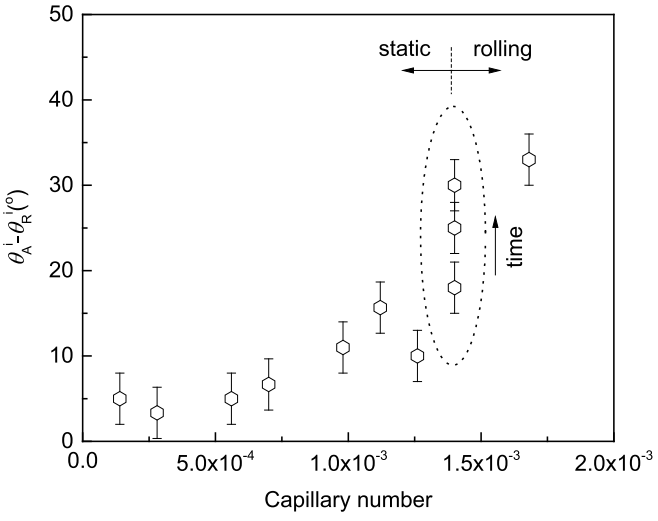

(b)

Fig. 6. (a) Contact angles of the droplet at the contact line and, (b) the difference between the contact angles for different Capillary numbers. The dotted ellipse indicates the region when droplet mobilisation starts.

The artificial compression velocity $\mathbf{U}_r$ in Eq. (5) is written as:

$$\mathbf{U}_r = \hat{\mathbf{n}} \cdot \min\left[C_\gamma \frac{|\phi|}{|S_f|}, \max\left(\frac{|\phi|}{|S_f|} \right) \right], \tag{8}$$

where ϕ is the mass flux, S_f is the surface area of the cell, and C_γ is an arbitrary compression coefficient. The max operation in Eq. (8) is performed over the entire domain, while the min operation is done locally at each face. The density field in Eqs. (3) and (4) is described as

$$\rho = \alpha \rho_{nw} + (1 - \alpha)\rho_w, \tag{9}$$

where ρ_{nw} and ρ_w are the density values of the two phases

A microchannel of $200 \times 50 \times 1600\ \mu m^3$ is chosen as the computation domain, where the cross section is the same as the test section in the experimental setup (Fig. 1). Due to the low Reynolds numbers ($Re < 1$), the inlet flow of the channel is considered fully developed with a parabolic velocity distribution. All solid walls are treated as no-slip and adiabatic. The distribution of the phase fractions at $t = 0$ is obtained from the experiments.

4.2. Numerical details

A major issue afflicting the VOF method is the inherent nonphysical spurious currents, which are induced by incorrect computations of the local curvature. To suppress the spurious currents, the following Laplacian filter introduced by Lafaurie et al. [42], which smoothens the phase function α [43,44], is used:

$$\widetilde{\alpha}_p = \frac{\sum_{f=1}^{n} \alpha_f S_f}{\sum_{f=1}^{n} S_f}, \tag{10}$$

where p and f denote the cell index and the face index, respectively. Then, the interface curvature in Eq. (6) is calculated with the smoothed phase function $\widetilde{\alpha}$ instead of α. The application of this smoother has been validated by Hoang et al. [43] to obtain an adequately smooth field for segmented flows in microchannels.

The PISO (Pressure-Implicit with Splitting of Operators) scheme was applied for the velocity–pressure coupling. The transient terms in the equations were discretised using a second-order implicit Crank-Nicolson scheme. The time step was chosen based on the maximum Courant number and the criterion for stable Capillary simulation suggested by Deshpande et al. [45]: $\Delta t \leqslant \min[\max(10\tau_\mu, 0.1\tau_\rho), \tau_{\mathrm{Co}_{\max}} = 0.1]$, where $\tau_\mu = \mu\Delta x/\sigma$ and $\tau_\rho = \sqrt{\mu\Delta x/\sigma}$. For spatial discretisation, a second-order total variation diminishing scheme with a van Leer limiter was used.

The main challenge for numerical simulations of droplet dynamics concerns the accurate description of the surface tension effects controlled by the contact angle hysteresis [46]. So far, many dynamic contact angle models have been developed, where θ_A and θ_R are usually described as a function of the contact line velocity and the equilibrium contact angle θ_E [47,48]. However, for the pinned droplet, where the contact line velocity is zero but the contact angles at the front (or quasi-advancing, θ_A^i) and back (or quasi-receding, θ_R^i) parts of the contact lines still differ from θ_E but are in the range of $\theta_A^i \leqslant \theta_A$ and $\theta_R^i \geqslant \theta_R$, the contact angles cannot be directly obtained from the available models. Therefore, an iterative procedure is used to determine the contact angles for the pinned droplet:

(1) Assume initial quasi-advancing and quasi-receding contact angles θ_A^i and θ_R^i, while θ_A^i and θ_R^i should ensure the equilibrium Young contact angle θ_E (using the model of Tadmor [9]). This has been proven by the experiments, as was shown in Section 3.
(2) Impose the assumed contact angles at the contact lines of the droplet, and run the numerical simulation to obtain the movement of the droplet under a given inlet channel velocity.
(3) If the contact line moves downstream, then increase the difference between θ_A^i and θ_R^i (and also ensure θ_E) and go to step 2.
(4) If the contact line moves upstream (though this is physically not reasonable), then decrease the difference between θ_A^i and θ_R^i and go to step 2.
(5) Iterate steps 2–5 to identify a set of θ_A^i and θ_R^i that enables the droplet to remain static on the solid surface.

Then, θ_A^i and θ_R^i are the contact angles at the quasi-advancing and quasi-receding parts, respectively, which results in the total forces balance on the droplet, for the considered numerical case. It should be noted that this numerical procedure can only be used for the simulation of a pinned droplet. If the droplet moves on the solid surface, a model for the dynamic contact angle should be used. The criterion of motion regime is determined by the contact angle hysteresis ($\theta_A - \theta_R$), which depends on the texture and the surface energies of the solid and the fluid [49,50], and is measured by experiments.

As a three-dimensional (3D) microchannel is considered in this study, the adhesion forces acting on the side walls may also play an important role in the droplet behaviour. To quantitatively understand that effect, the simulations are performed in both two and three dimensions. In the 2D simulation, the solid–water interface is a straight line along the top wall, where θ_A^i and θ_R^i can be imposed directly on the front and rear contact lines, respectively. However, in the 3D simulation, the contact line is much more complex, existing on the top, front, and back walls. Furthermore, information on the front and back walls is very difficult to obtain experimentally, as was also pointed out previously by Fang et al. [51]. Therefore, we divide the contact lines on each side wall into two parts, according to the coordinate of the cell: $x > x_m$ and $x \leqslant x_m$, where x_m is the location of the mass center of the droplet on the x–axis. The contact angle at $x \leqslant x_m$ is chosen to be the same as θ_R^i and that at $x > x_m$ is imposed as θ_A^i during the iterations. This simplified method has also been used in some previous numerical models [13,14,52] to consider the effect of the contact angle hysteresis.

The flow domains were meshed with uniform hexahedral cells. A grid sensitivity study was performed to select the proper number of grid cells. The results of the dependence of numerical accuracy and spurious current on grid sizes and the validation of the present numerical models will be discussed in detail in Section 5.

5. Numerical results

As the internal circulation motion of the droplet is sensitive to nonphysical spurious currents, efforts are made to reduce them. The relaxation of a 3D stationary droplet from a half-cylinder shape on hydrophobic bounded walls (with contact angles of 126°) is simulated first to evaluate the effect of the Laplacian smoother of the phase field (Eq. (10)). Fig. 7 shows the vectors of the spurious currents near the static droplet adhering to a solid wall with and without using the smoother. The fluid properties are the same as in the experiments, with uniform numerical grid size $H/\Delta = 64$ (H is the channel height and Δ is the size of each grid cell)). It is found that the magnitudes of the velocity inside and outside of the droplet decrease obviously when the smoother is

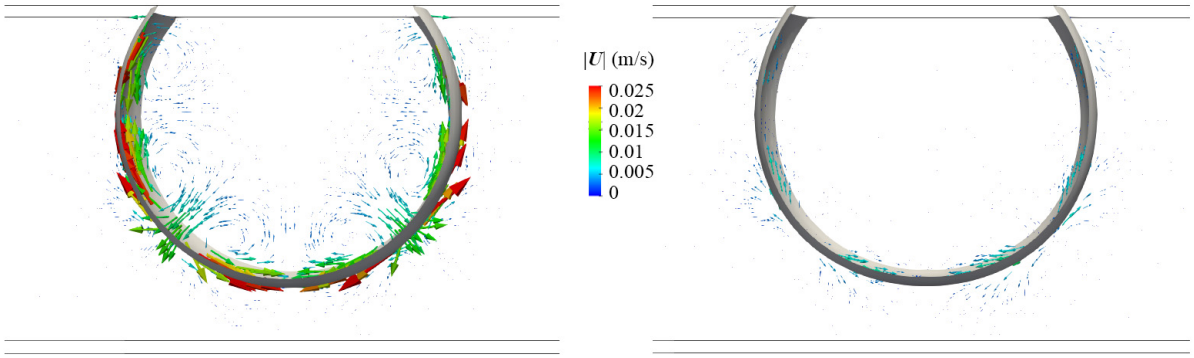

Fig. 7. Spurious currents around a static droplet obtained by simulations without and with using of the phase smoother.

used. The effects of the number of repeated sweeps of the smoother and the grid size on the magnitude of the spurious currents are further investigated to choose adequate parameters. As shown in Fig. 8, the maximum spurious currents in the wetting and non-wetting phases as well as their averaged values in the droplet decrease monotonically with the increasing sweep numbers, where the decrease is quite abrupt for sweep numbers from 0 to 1. Such a trend is similar to that reported by Hoang et al. [43] for a 2D, stationary, circular droplet. The effect of grid size on the spurious currents is also presented in this figure, which shows that it is less important than the use of the smoother function. Different grids ($H/\Delta = 50$, $H/\Delta = 64$, $H/\Delta = 80$, and $H/\Delta = 100$) are also tested to simulate one of the droplet pinned cases with a channel flow ($Ca = 1.12 \times 10^{-3}$). The effect of grid size on the numerical results has been found to be negligible as the maximum recirculation velocity inside the droplet has the same value if three significant digits are kept. Therefore, a smoothing sweep number of 2 and a grid size of $H/\Delta = 64$ are used in all remaining simulations in this study.

Fig. 9 shows a typical velocity distribution within a drop pinned to the hydrophobic surfaces of a microfluidic channel as a result of contact angle hysteresis for a Capillary number of $Ca = 1.33 \times 10^{-3}$. The results are obtained after the wetting phase flow and the phase field become stable. Based on the shape, the droplet can be considered static, as the contact line and the interface locations are both fixed. However, this does not mean the fluid inside the droplet is also static, as a circulation flow field can be clearly observed in the middle plane of the droplet, with a vortex core located in the lower part of the droplet. Such a phenomenon is in accordance with the experimental observations shown previously in Section 3. Furthermore, it can be found that all velocity vectors at the interface are tangential to the interface, which ensures the stationarity of the droplet shape.

The distributions of the x-component of the velocity, normalized by the maximum wetting phase velocity, along the vertical line across the center of the droplet obtained by a 3D simulation, a 2D simulation (without the front and back walls), and experimental results for $Ca = 1.12 \times 10^{-3}$ are presented in Fig. 10. A similar velocity variation along y can be found, where the velocity in the droplet is negative above the vortex core while it is positive below the vortex core. The maximum local velocity magnitude is located near the water–Fluorinert interface. Compared to the 2D simulation, the results from the 3D simulation show a better agreement with the experiments. The predicted droplet cross-section is more circular in the 2D simulation than in the 3D simulation, while both of them have a more circular shape than that from the experimental observation. This error might be induced by the simplification of the implementation of the contact angle models at the side walls. This variation trend is also found in the predicted contact angles. Fig. 11 presents a comparison of the difference of the quasi-advancing and quasi-receding contact angles ($\theta_A^i - \theta_R^i$) obtained by the experiments and the numerical simulations for various Capillary numbers. The value of ($\theta_A^i - \theta_R^i$) is shown to increase with increasing Capillary number, and the 3D simulation results are closer to the experimental ones. The results are higher in the 2D simulation for each case, as is expected, because the adhesion forces on the front and back walls are omitted and only the force at the top wall balances the drag force from the channel flow. The 3D simulations can also well predict the location of the vortex core of the rotating fluid in the droplet for different Capillary numbers, as shown in Fig. 12. The vortex core moves slightly upward along the y–direction as the Capillary number increases, and the difference between the 3D simulations and experiments are within 10%.

6. Force analysis

The force analysis for the pinned droplet is performed based on the 3D simulation results for various Capillary numbers. The forces on the droplet pinned to the surfaces of a confined microfluidic channel consist of drag force and adhesion force (surface tension force), as shown schematically in Fig. 13. The force of gravity is negligible because of the small length scale. The drag force, exerted by the wetting phase around the droplet, is the sum of the pressure and viscous forces:

$$F_{\text{drag}} = F_p + F_\mu. \tag{11}$$

The pressure force arises from the pressure difference between the upstream and downstream ends of the droplet. If we consider the force balance in the flow direction (x), the pressure force can be calculated by using

$$F_{p,x} = \hat{\mathbf{e}}_x \cdot \int_A \hat{\mathbf{n}} P dA, \tag{12}$$

where $\hat{\mathbf{e}}_x$ is the direction vector of the channel flow, and A is the interface area. The viscous force is caused by the gradient of velocity of the wetting fluid near the droplet surface, the component of which in the flow direction is calculated by

$$F_{\mu,x} = \hat{\mathbf{e}}_x \cdot \int_A \mu_w \hat{\mathbf{n}} \cdot \nabla \mathbf{U} dA. \tag{13}$$

As the droplet contacts top and side solid walls, the adhesion force consists of two parts. The adhesion force at the top wall can be calculated by

$$\sum F_{\gamma,x,\text{top}} = \hat{\mathbf{e}}_x \cdot \int_{\text{CL}_A,\text{top}} \hat{\mathbf{n}} \gamma_{nw-w} \cos\theta_A^i dS - \hat{\mathbf{e}}_x \cdot \int_{\text{CL}_R,\text{top}} \hat{\mathbf{n}} \gamma_{nw-w} \cos\theta_R^i dS \tag{14}$$

where CL donates the contact line domain. The adhesion force at the side walls (front and back) can be calculated by using

$$\sum F_{\gamma,x,\text{side}} = 2\left(\hat{\mathbf{e}}_x \cdot \int_{\text{CL}_{x>x_m},\text{front}} \hat{\mathbf{n}} \gamma_{nw-w} \cos\theta_A^i dS - \hat{\mathbf{e}}_x \cdot \int_{\text{CL}_{x<x_m},\text{front}} \hat{\mathbf{n}} \gamma_{nw-w} \cos\theta_R^i dS \right) \tag{15}$$

The results of Eqs. (11)–(15) have been obtained by the integration of numerical results of pressure, velocity, or phase fraction values on each grid cell.

Fig. 14 presents the calculation results of all force components on the droplet for various Capillary numbers. The net force for each case is zero, as the droplet is pinned to the surfaces. This also proves the accuracy of the force calculation from the numerical data. For all cases considered in this study, the driving force is dominated by the pressure force rather than the viscous force. The viscous force is only 2.07%of the pressure force for a Capillary number of 2.80×10^{-4}, which decreases to 1.66% when the capillary number increases to 1.12×10^{-3}. The adhesion

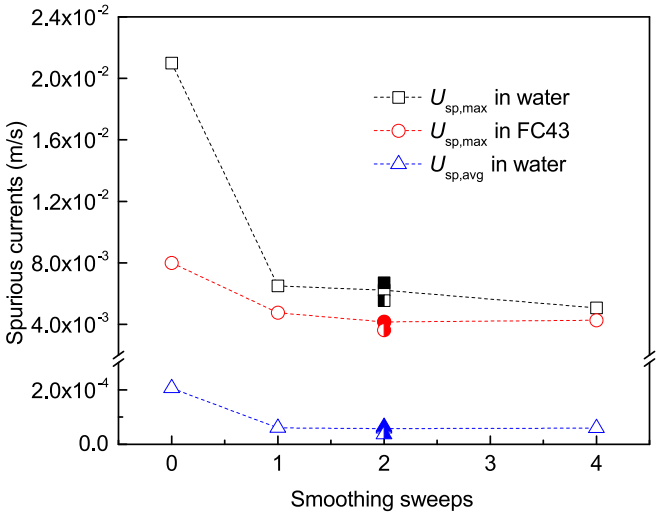

Fig. 8. Variation in the spurious currents for a steady droplet with repeated sweep times of the smoother function. (Hollow symbols: $H/\Delta = 64$; filled symbols: $H/\Delta = 50$; half-filled symbols: $H/\Delta = 100$.).

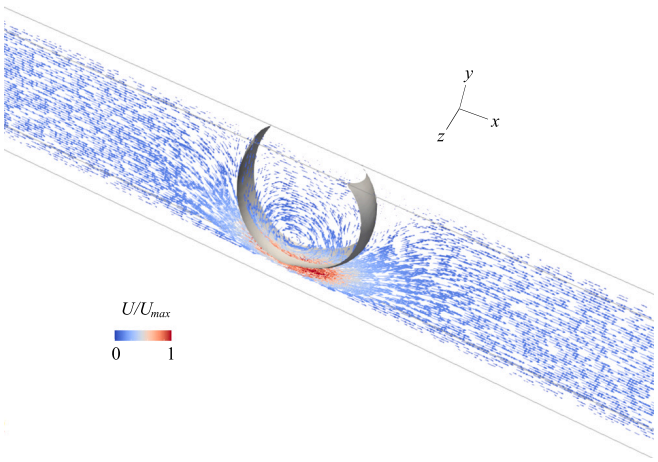

Fig. 9. Representative velocity vectors inside the pinned droplet and in the surrounding flow obtained by numerical simulation (U_{max} = 0.09 m/s).

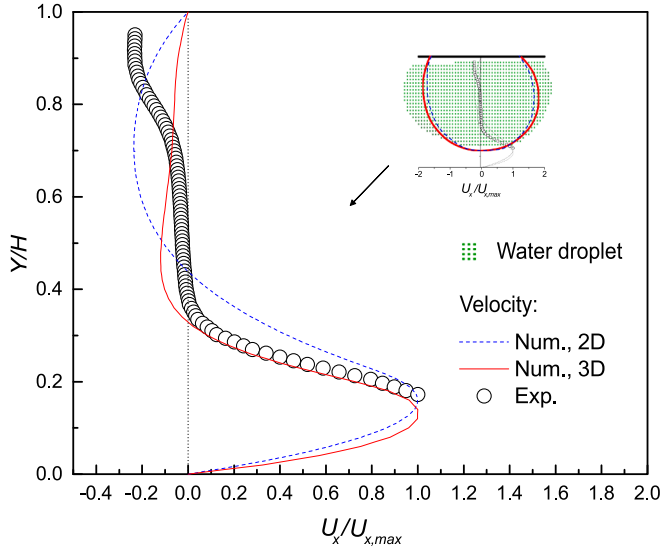

Fig. 10. Comparison of the local velocity distributions inside the droplet obtained by experiment and numerical simulations.

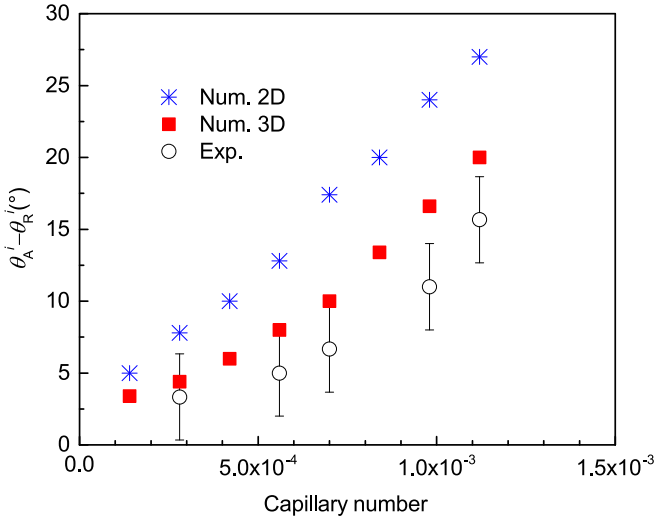

Fig. 11. Comparison of ($\theta_A^i - \theta_R^i$) obtained by experiment and numerical simulations.

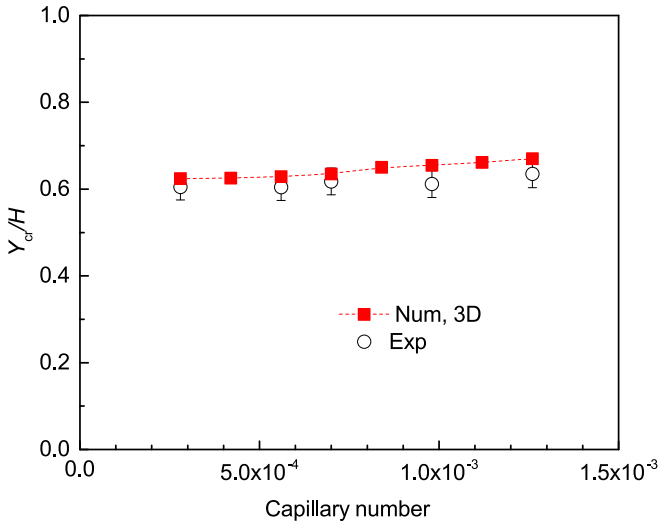

Fig. 12. Location of the vortex core of the rotating fluid in the droplet.

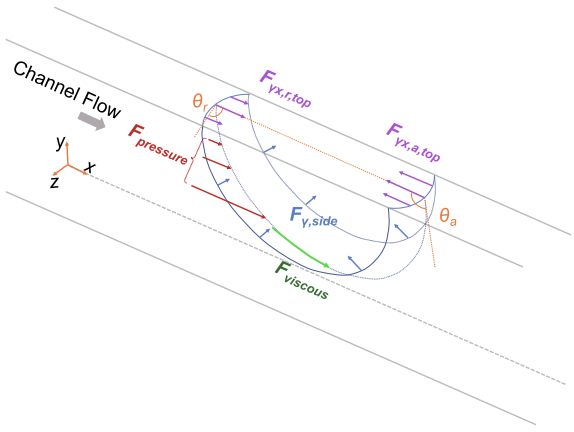

Fig. 13. Schematic of the forces on a water droplet pinned to the surfaces of a confined microchannel.

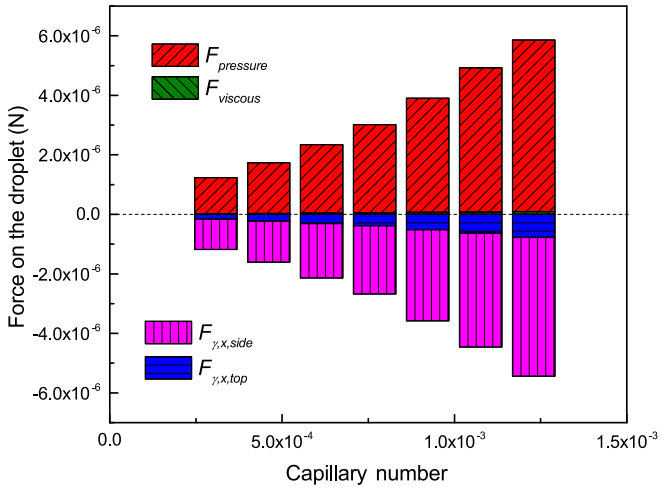

Fig. 14. Variation in the force components on the droplet with Capillary number.

force induced by the contact angle hysteresis increases with increasing capillary force to maintain the stationarity of the droplet. The adhesion force at the side walls is by a factor of about ~6 larger than that at the top wall, because of the longer contact line at the side walls. This also explains why a larger error can be introduced by the 2D simulations, as shown previously in Section 5.

To further investigate the relationship between the drag force and wetting phase flow velocity, the drag coefficient on the droplet in the microfluidic channel is calculated based on the following equation:

$$C_D = \frac{F_{\text{drag}}}{\frac{1}{2}\rho_w \overline{U}_w^2 E_d}, \tag{16}$$

where E_d is the projected area of the droplet orthogonal to the x-axis in the channel flow. The drag coefficients are also compared with analytical correlations from literature. It is well known that, if the Reynolds number governing the flow is low, the drag coefficient is given by the Stokes drag:

$$C_{D,St} = \frac{24}{\text{Re}}. \tag{17}$$

where $Re = \rho_w \overline{U}_w h/\mu_w$, and h is the average height of the droplet. The Stokes drag is applicable for a creeping flow regime with Re < 0.4. Including the effect of inertia, Oseen [53] developed a correction to the Stokes drag:

$$C_D = C_{D,St}\left(1 + \frac{3}{16}\text{Re}\right). \tag{18}$$

As shown in Fig. 15(a), the drag coefficients obtained by Eqs. (17) and (18) and by the present simulation of Eq. (16) all decrease with increasing Reynolds number. The difference between Stokes drag and Oseen's correction is small, as the Reynolds number in this study is always less than 1, which indicates the inertia force is weak. However, the drag coefficient based on the present simulation is more than two orders of magnitude higher than predicted by the correlations Eqs. (17) and (18). This is because these correlations are suitable only for a droplet in a free–stream flow, but in a microchannel flow, the droplet size is comparable to the channel size, and the blockage effect of the droplet on the channel flow should also be considered. Therefore, a correlation factor should be considered by taking into account the confinement effect to use these analytical correlations such as Eqs. (17) and (18).

Fig. 15(b) shows the variation in the confinement correction factor (ratio between the drag coefficients in confined and unconfined flows). As reported previously by Quddus et al. [54], the confinement correction factor should only be a function of the ratio of the droplet projected area to the channel cross-sectional area. As the projected area of the droplet is found to slightly decrease with increasing Reynolds number, the confinement correction factor also increases. The confinement correction factor for the present model increases from 118.6 to 157.3, when the Reynolds number increases from 0.20 to 0.87. Moreover, good agreement can be found between the present confinement correction factor and that by Quddus et al. [54]. It should be noted that in some recent analytical models [22,21] for droplet motion, the drag coefficient models were used without considering such confinement effects. Our study shows that this omission may lead to significant errors when predicting droplet motion in a microfluidic channel.

From the above-mentioned force balance model, the contact angles of a pinned droplet in a microchannel can be predicted: First, the drag force can be calculated from information of the channel wetting phase flow by combining the confinement correction factor and the drag coefficient models; then, the adhesion force can be obtained according to the force balance, and the advancing and receding contact angles are inversely solved from the adhesion force equations (Eq. 14 and 15).

7. Intensity of the internal circulation

Although the total force acting on the droplet is balanced, a torque still exists; this torque leads to the internal circulation behavior of liquids within the droplet (Fig. 9). Fig. 16 shows the distribution of x-component of velocity at the vertical cross section of the microchannel (200 × 50 μm) through the mass center of the droplet for Capillary numbers of 4.20×10^{-4} and 1.12×10^{-3}. For both cases, the droplet is pinned to the surfaces as a result of the contact angle hysteresis. Therefore, the velocities at the contact lines are zero, which leads to a nonuniform angular velocity inside the droplet. The torque analysis cannot be performed by taking the droplet as a rigid object, as done for the rolling droplets along the surfaces [25,55]. For the latter case, the angular velocity has been assumed to be uniform everywhere in the droplet in previous analytical models. The circulation within the droplet is more complex for the pinned case, as the viscous force inside the water droplet also has an effect on the circulation intensity. From Fig. 16, an increase in the projected area of the droplet with the Capillary number can also be found, which is in accordance with the experiments.

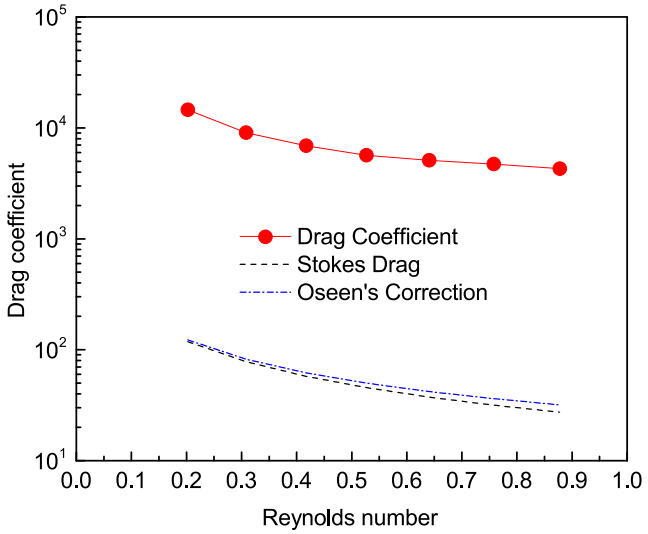

(a) Drag coefficient

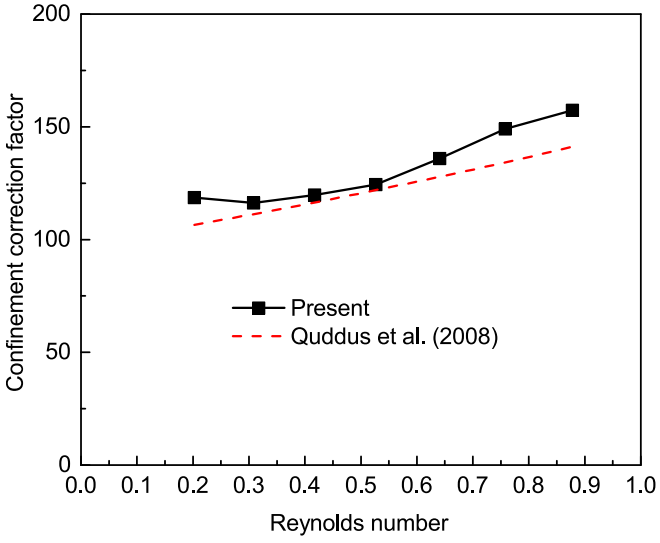

(b) Confinement correction factor

Fig. 15. Drag coefficient on the droplet and its correction with the blockage effect on the channel flow taken into account.

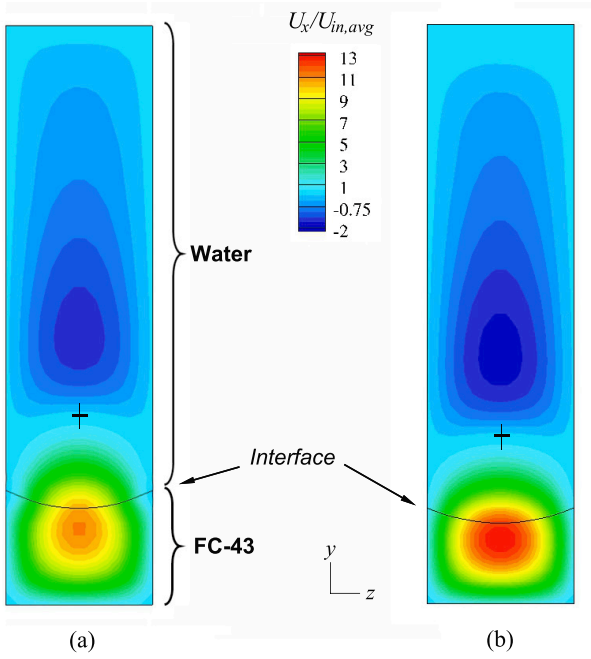

Fig. 16. Distribution of the *x*-component velocity at the spanwise cross section of the microchannel through the vortex core for (a) $Ca = 4.20 \times 10^{-4}$ and (b) $Ca = 1.12 \times 10^{-3}$. (The black crosses indicate the vortex cores.).

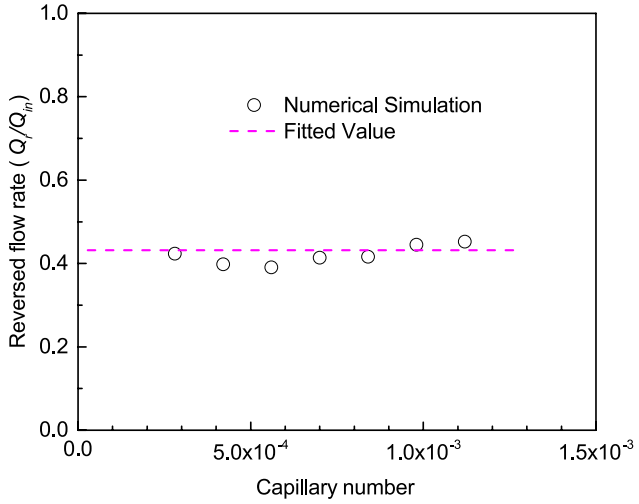

Fig. 17. Reversal flow rates inside the droplet for various Capillary numbers.

As the droplet shown in Fig. 16 is stationary, the flow rates inside the droplet in streamwise and opposite directions should be equal (both volume and mass flow rates, as the water density is considered constant). Fig. 17 presents the variation in the normalized volumetric flow rate of the reversed flow at the same cross–section shown in Fig. 16 for various Capillary numbers. As the Capillary number increases, the flow rate of the reversed flow, normalized by the channel inlet flow rate, is almost constant. Therefore, the intensity of the internal rotation can be correlated by the following equation with a good fit:

$$Q_r/Q_{in} = 0.4345 \tag{19}$$

Eq. (19) is valid for $Ca < 1.2 \times 10^{-3}$ and the R-squared value is 0.987.

8. Concluding remarks

The determination of droplet motion in a microchannel is of great significance in a wide range of applications in chemical engineering. In this study, the fluid dynamics inside a water droplet pinned to the solid surfaces of a microchannel has been experimentally and numerically investigated. The internal circulation of the droplet has been observed by means of a micro-PIV system; this circulation has also been simulated successfully using a modified VOF method.

For small Capillary numbers, the droplet is pinned at the solid hydrophobic surfaces, because of the unbalanced surface tension force caused by the contact angle hysteresis effect. As the Capillary number exceeds a critical value, the droplet starts to roll along the surface. It is found from the experiments that, for the pinned droplet, the contact angle increases at the front part and decreases at the rear part with an increase in Capillary number. The equilibrium Young's contact angles calculated from them, are almost constant.

Spurious currents from the VOF method are reduced by using a Laplacian filter for the phase function, which makes it possible to simulate the internal circulation flow in the numerical simulations. Major quantities from the simulations, including the internal velocity distribution, contact angles, and vortex structures, show overall good agreement with experimental results. Furthermore, results from 3D simulations agree much better than those from 2D simulations.

A force balance analysis indicates that the adhesion force at the side walls and the blockage of the droplet of the channel flow may have significant effects on droplet motion and should not be omitted in theoretical models. For a pinned droplet, the projected area of the droplet increases with increasing Capillary numbers, and the circulation flow rate inside the droplet varies linearly with Capillary number.

Acknowledgments

The authors would like to acknowledge the German Research Foundation (DFG) for funding support within the SFB 1313 and GRK 2160 research projects. The authors also thank Christoph Sürgers and Sihao Deng from the Physikalisches Institut at Karlsruhe Institute of Technology (KIT) for assistance with the AFM tests. A. Terzis also acknowledges the Alexander von Humboldt (AvH) foundation for the funding support.

References

[1] B. Bhushan, K. Koch, Y.C. Jung, Nanostructures for superhydrophobicity and low adhesion, Soft Matter 4 (9) (2008) 1799–1804.
[2] J. Cao, B. Donell, D.R. Deaver, M.B. Lawrence, C. Dong, In VitroSide-view imaging technique and analysis of human T-leukemic cell adhesion to ICAM-1 in shear flow, Microvascular Res. 55 (2) (1998) 124–137.
[3] E.N. Tummons, V.V. Tarabara, J.W. Chew, A.G. Fane, Behavior of oil droplets at the membrane surface during crossflow microfiltration of oil-water emulsions, J. Membr. Sci. 500 (2016) 211–224.
[4] P. Gopalan, S.G. Kandlikar, Investigation of water droplet interaction with the sidewalls of the gas channel in a PEM fuel cell in the presence of gas flow, ECS Trans. 41 (1) (2011) 479–488.
[5] P. Dimitrakopoulos, J. Higdon, Displacement of fluid droplets from solid surfaces in low-Reynolds-number shear flows, J. Fluid Mech. 336 (1997) 351–378.
[6] A. Payatakes, Dynamics of oil ganglia during immiscible displacement in water-wet porous media, Annu. Rev. Fluid Mech. 14 (1) (1982) 365–393.
[7] R. Seemann, M. Brinkmann, T. Pfohl, S. Herminghaus, Droplet based microfluidics, Rep. Progress Phys. 75 (1) (2011) 016601.
[8] S. Sharma, M. Srisa-Art, S. Scott, A. Asthana, A. Cass, Droplet-based microfluidics (2013) 207–230.
[9] R. Tadmor, Line energy and the relation between advancing, receding, and young contact angles, Langmuir 20 (18) (2004) 7659–7664.
[10] Q. Kang, D. Zhang, S. Chen, Q. Kang, Displacement of a two-dimensional immiscible droplet in a channel Displacement of a two-dimensional immiscible droplet in a channel, Phys. Fluids 14 (2002) 3203.
[11] P. Dimitrakopoulos, Deformation of a droplet adhering to a solid surface in shear flow: onset of interfacial sliding, J. Fluid Mech. 580 (2007) 451–466.
[12] H. Ding, M.N. Gilani, P.D. Spelt, Sliding, pinch-off and detachment of a droplet on a wall in shear flow, J. Fluid Mech. 644 (2010) 217–244.
[13] M. Mahé, M. Vignes-Adler, A. Rousseau, C. Jacquin, P. Adler, Adhesion of droplets on a solid wall and detachment by a shear flow: I. Pure systems, J. Colloid Interface Sci. 126 (1) (1988) 314–328.
[14] B. Blackmore, D. Li, J. Gao, Detachment of bubbles in slit microchannels by shearing flow, J. Colloid Interface Sci. 241 (2) (2001) 514–520.
[15] Q. Kang, D. Zhang, S. Chen, Displacement of a two-dimensional immiscible droplet in a channel, Phys. fluids 14 (9) (2002) 3203–3214.

[16] E. Kumbur, K. Sharp, M. Mench, Liquid droplet behavior and instability in a polymer electrolyte fuel cell flow channel, J. Power Sources 161 (1) (2006) 333–345.
[17] G. Seevaratnam, H. Ding, O. Michel, J. Heng, O. Matar, Laminar flow deformation of a droplet adhering to a wall in a channel, Chem. Eng. Sci. 65 (16) (2010) 4523–4534.
[18] J. Fan, M. Wilson, N. Kapur, Displacement of liquid droplets on a surface by a shearing air flow, J. Colloid Interface Sci. 356 (1) (2011) 286–292.
[19] I. Zarikos, A. Terzis, S. Hassanizadeh, B. Weigand, Velocity distributions in trapped and mobilized non-wetting phase ganglia in porous media, Sci. Rep. 8 (1) (2018) 13228.
[20] S.P. Thampi, R. Adhikari, R. Govindarajan, Do liquid drops roll or slide on inclined surfaces? Langmuir 29 (10) (2013) 3339–3346.
[21] S.C. Cho, Y. Wang, K.S. Chen, Droplet dynamics in a polymer electrolyte fuel cell gas flow channel: forces, deformation, and detachment. I: Theoretical and numerical analyses, J. Power Sources 206 (2012) 119–128.
[22] J. Xie, J. Xu, W. Shang, K. Zhang, Mode selection between sliding and rolling for droplet on inclined surface: effect of surface wettability, Int. J. Heat Mass Transf. 122 (2018) 45–58.
[23] D.R. Reyes, D. Iossifidis, P.-A. Auroux, A. Manz, Micro total analysis systems. 1. Introduction, theory, and technology, Anal. Chem. 74 (12) (2002) 2623–2636.
[24] S.R. Annapragada, J.Y. Murthy, S.V. Garimella, Prediction of droplet dynamics on an incline, Int. J. Heat Mass Transf. 55 (2012) 1466–1474.
[25] B.S. Yilbas, A. Al-Sharafi, H. Ali, N. Al-Aqeeli, Dynamics of a water droplet on a hydrophobic inclined surface: influence of droplet size and surface inclination angle on droplet rolling, RSC Adv. 7 (77) (2017) 48806–48818.
[26] B.S. Yilbas, G. Hassan, A. Al-Sharafi, H. Ali, N. Al-Aqeeli, A. Al-Sarkhi, Water droplet dynamics on a hydrophobic surface in relation to the self-cleaning of environmental dust, Sci. Rep. 8 (1) (2018) 2984.
[27] S. Tasoglu, G. Kaynak, A.J. Szeri, U. Demirci, M. Muradoglu, Impact of a compound droplet on a flat surface: a model for single cell epitaxy, Phys. Fluids 22 (8) (2010) 082103.
[28] H. Kinoshita, S. Kaneda, T. Fujii, M. Oshima, Three-dimensional measurement and visualization of internal flow of a moving droplet using confocal micro-PIV, Lab Chip 7 (3) (2007) 338–346.
[29] Z. Liu, L. Zhang, Y. Pang, X. Wang, M. Li, Micro-PIV investigation of the internal flow transitions inside droplets traveling in a rectangular microchannel, Microfluid. Nanofluid. 21 (12) (2017) 180.
[30] V.S. Cabeza, S. Kuhn, A.A. Kulkarni, K.F. Jensen, Size-controlled flow synthesis of gold nanoparticles using a segmented flow microfluidic platform, Langmuir 28 (17) (2012) 7007–7013.
[31] N.K. Karadimitriou, M. Musterd, P.J. Kleingeld, M.T. Kreutzer, S.M. Hassanizadeh, V.J. Niasar, On the fabrication of PDMS micromodels by rapid prototyping, and their use in two-phase flow studies, Water Resour. Res. 49 (4) (2013) 2056–2067.
[32] I.M. Zarikos, S.M. Hassanizadeh, L.M. van Oosterhout, W. van Oordt, Manufacturing a micro-model with integrated fibre optic pressure sensors, Transp. Porous Media 122 (1) (2018) 221–234.
[33] P. Garstecki, M.J. Fuerstman, H.A. Stone, G.M. Whitesides, Formation of droplets and bubbles in a microfluidic T-junction—scaling and mechanism of break-up, Lab Chip 6 (3) (2006) 437–446.
[34] B. Chen, F. Guo, G. LI, P. Wang, Three-dimensional simulation of bubble formation through a microchannel T-junction, Chem. Eng. Technol. 36 (12) (2013) 2087–2100.
[35] W. Thielicke, E. Stamhuis, PIVlab – Towards user-friendly, affordable and accurate digital particle image velocimetry in MATLAB, J. Open Res. Softw. 2 (1) (2014) 1202.
[36] O. Uzol, C. Camci, The effect of sample size, turbulence intensity and the velocity field on the experimental accuracy of ensemble averaged PIV measurements, in: 4th International Symposium on Particle Image Velocimetry, Göttingen, Germany, September 17-19, 2001, 2001.
[37] C. Extrand, Contact angles and their hysteresis as a measure of liquid- solid adhesion, Langmuir 20 (10) (2004) 4017–4021.
[38] K. Grundke, Surface-energetic properties of polymers in controlled architecture, Molecular Interfacial Phenomena of Polymers and Biopolymers, Elsevier, 2005, pp. 323–374.
[39] Y. Yonemoto, S. Suzuki, S. Uenomachi, T. Kunugi, Sliding behaviour of water-ethanol mixture droplets on inclined low-surface-energy solid, Int. J. Heat Mass Transf. 1315–1324 (120) (2018) 0017–9310.
[40] L. Makkonen, J. Kurkela, Another look at the interfacial interaction parameter, J. Colloid Interface Sci. 529 (2018) 243–246.
[41] J. Brackbill, D.R. Kothe, C. Zemach, A continuum method for modeling surface tension, J. Comput. Phys. 100 (1992) 335–354.
[42] B. Lafaurie, C. Nardone, R. Scardovelli, S. Zaleski, G. Zanetti, Modelling merging and fragmentation in multiphase flows with SURFER, J. Comput. Phys. 113 (1) (1994) 134–147.
[43] D.A. Hoang, V. van Steijn, L.M. Portela, M.T. Kreutzer, C.R. Kleijn, Benchmark numerical simulations of segmented two-phase flows in microchannels using the Volume of Fluid method, Comput. Fluids 86 (2013) 28–36.
[44] K. van As, https://github.com/floquation/OF-kva_interfaceProperties, 2017.
[45] S.S. Deshpande, L. Anumolu, M.F. Trujillo, Evaluating the performance of the two-phase flow solver interFoam, Comput. Sci. Discovery 5 (1) (2012) 014016.
[46] J.-B. Dupont, D. Legendre, Numerical simulation of static and sliding drop with contact angle hysteresis, J. Comput. Phys. 229 (7) (2010) 2453–2478.
[47] R. Cox, The dynamics of the spreading of liquids on a solid surface. Part 1. Viscous flow, J. Fluid Mech. 168 (1986) 169–194.
[48] S. Afkhami, S. Zaleski, M. Bussmann, A mesh-dependent model for applying dynamic contact angles to VOF simulations, J. Comput. Phys. 228 (15) (2009) 5370–5389.
[49] R.E. Johnson Jr, R.H. Dettre, Contact angle hysteresis. III. Study of an idealized heterogeneous surface, J. Phys. Chem. 68 (7) (1964) 1744–1750.
[50] J.-H. Song, M. Sakai, N. Yoshida, S. Suzuki, Y. Kameshima, A. Nakajima, Dynamic hydrophobicity of water droplets on the line-patterned hydrophobic surfaces, Surface Sci. 600 (13) (2006) 2711–2717.
[51] C. Fang, C. Hidrovo, F.-M. Wang, J. Eaton, K. Goodson, 3-D numerical simulation of contact angle hysteresis for microscale two phase flow, Int. J. Multiph. Flow 34 (7) (2008) 690–705.
[52] G. Ahmed, M. Sellier, M. Jermy, M. Taylor, Modeling the effects of contact angle hysteresis on the sliding of droplets down inclined surfaces, Eur. J. Mech.-B/Fluids 48 (2014) 218–230.
[53] C.W. Oseen, Hydrodynamik, vol. 1, Akademische Verlagsgesellschaft, 1927.
[54] N.A. Quddus, W.A. Moussa, S. Bhattacharjee, Motion of a spherical particle in a cylindrical channel using arbitrary Lagrangian-Eulerian method, J. Colloid Interface Sci. 317 (2008) 620–630.
[55] L. Mahadevan, Y. Pomeau, Rolling droplets, Phys. Fluids 11 (9) (1999) 2449–2453.